

NON-PLANE WAVE SCATTERING FROM A SINGLE ECCENTRIC CIRCULAR INCLUSION – PART I: SH WAVES

WOLFGANG WEBER
BERND W. ZASTRAU

Technische Universität Dresden, Dresden, Germany
e-mail: wolfgang.weber@tu-dresden.de

In this contribution, an analytical formalism for investigating the scattering behaviour of a single multi-layered inclusion in a homogeneous isotropic matrix under the influence of non-plane elastic SH waves is derived. Herein, the inclusion is assumed to have a circular shape with its layers being eccentrically arranged. Numerical examples are performed with Textile Reinforced Concrete, a new building material in civil engineering. Within these investigations both shielding and amplification of SH waves is shown.

Key words: non-plane waves, scattering, eccentric scatterer, SH wave, elastic wave, TRC

1. Introduction

In many applications in civil, mechanical, biological engineering and related disciplines, investigations concerning the dynamical behaviour of structures or parts of them are regularly necessary as they are exposed to dynamic loads. These may be time-harmonic loads as they occur with rotating machines mounted at floor slabs or transient loads due to e.g. impacts. The corresponding engineer is then interested in the structures response. For these investigations at the so-called macro- or structural-scale, profound insight into the materials behaviour at the micro- and meso-scale is necessary in order to develop adequate mechanical models which allow efficient calculations with a specified accuracy. In real-life applications these forecasts or simulations are made complicated by the fact that both the material and geometric properties of the structure and its constituents as well as the dynamic loads themselves

may vary. Hence, capable solutions including their efficient numerical implementation are required to fit the needs arising from numerical studies on the micro- or meso-scale.

In what follows, the wave scattering behaviour of a single inhomogeneous inclusion embedded in a homogeneous matrix of infinite extent is investigated. Herein, the matrix material is supposed to behave linear elastic and isotropic. The calculations are performed with elastic waves propagating through the textile reinforced concrete (TRC), a new construction material in civil engineering consisting of a fine grained concrete matrix with a maximum grain size of approx. 0.6 mm and fibres made of glass or carbon which are warp-knitted to uni- or multiaxial reinforcement clutches and then are worked in the fine grained concrete matrix, cf. Ortlepp and Curbach (2009). These fibres, which are often called rovings as well, consist of 800 up to 2000 filaments, each with a diameter of approx. $13.5 \mu\text{m}$. A view in the direction of the fibres as shown in Fig. 1 gives rise to the assumption that the single filaments do participate differently in the load bearing behaviour. In detail, the outer filaments have

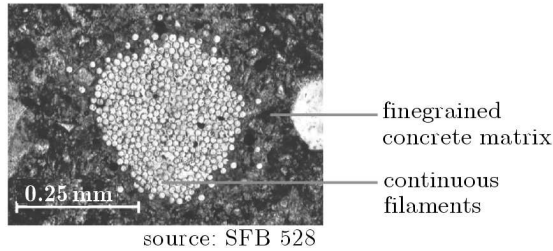


Fig. 1. Setup of a roving

a better interconnection to the surrounding matrix than the inner ones. For some models concerning the decreasing degree of bonding see e.g. Lepenies (2007). Additionally, the matrix behaviour in the vicinity of the rovings will differ from the undisturbed matrix. Consequently, the inclusion – which acts as an obstacle for the incoming (non-plane) wave and thus will scatter it – is modeled as a double-layered scatterer. Herein the inner layer is the roving corresponding to the inner filaments. Thus, it can be called the (inner) core as well. On the other hand, the outer layer is motivated by the interphase between the outer filaments and the matrix in the vicinity of the fibre. Among other things, due to the production and curing process of TRC the inner and outer layer will be eccentric in most cases, see Weber and Zastrau (2010). In the following, an analytical solution for the scattering of non-plane shear waves by eccentric layered inclusions is derived and some numerical results for arbitrarily chosen deterministic frequencies are discussed. Other parameters

influencing the wave scattering behaviour of the example dealt with here are uncertainties in the material properties (e.g. Young's modulus, Poisson's ratio) and the dynamic loads (i.e. amplitude, frequency).

2. Some general remarks on elastic waves

Based on Navier's equation without body forces

$$\mu \Delta \mathbf{u} + (\lambda + \mu) \nabla \nabla \cdot \mathbf{u} = \rho \ddot{\mathbf{u}} \quad (2.1)$$

with $\Delta = \nabla^2$, $\mathbf{u} = (u, v, w)$ displacement vector, λ , μ Lamé constants and ρ the density of the material at hand, two general wave types can be distinguished according to Fig. 2: the so called *S* wave is connected to the direction of particle motion \mathbf{d} perpendicular to the direction of wave propagation (the wave normal \mathbf{n}) whereas in the P wave case the direction of particle motion is parallel to the wave normal. Hence, the P wave is referred to as *pressure* wave and the S wave as *shear* wave. Both waves have different propagation speeds. The (longitudinal) P wave propagates with $c_L = \sqrt{(\lambda + 2\mu)/\rho}$, the (transverse) S wave with $c_T = \sqrt{\mu/\rho}$, respectively. As $c_L > c_T$ the P wave is called *primary* wave as well – and hence S wave can be understood as *secondary* wave, see e.g. Achenbach (1973). Obviously these propagation speeds c are characteristic for a certain material and so is the wave number k

$$k = \frac{\omega}{c} \quad (2.2)$$

where ω is the circular frequency of the wave, cf. Cai (2004). In general, the impinging of one wave type – either P or S wave – upon the surface of an elastic body or an obstacle induces both wave types in the reflection problem (or additional two waves in the case of refracted waves), see Fig. 2. The S wave

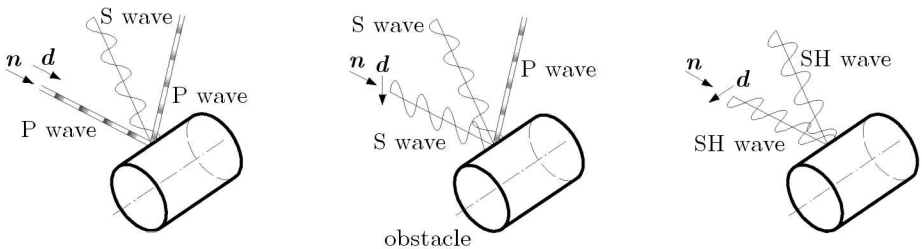


Fig. 2. Mode conversion, using the example of reflection of waves

can be decomposed into a SV and a SH wave, where SV means a vertically polarised shear wave and SH a horizontally polarised shear wave, respectively. If the direction of particle motion is parallel to the axis of the obstacle, a SH wave is at hand, see Fig. 2. It is characteristic that a SH wave is reflected (and refracted) as a SH wave only. For the sake of brevity, this special case will be evaluated throughout this paper.

An eccentric layered elastic circular cylinder which is embedded in a linear elastic and isotropic medium of infinite extent as depicted in Fig. 3b with different wave numbers k_m , k_{iph} , and k_{fi} is considered. Herein and with other parameters the subscripts m , iph , and fi hold with the matrix, the interphase and the fibre, respectively. The resulting waves are sought due to the acting of a time-harmonic incident SH wave.

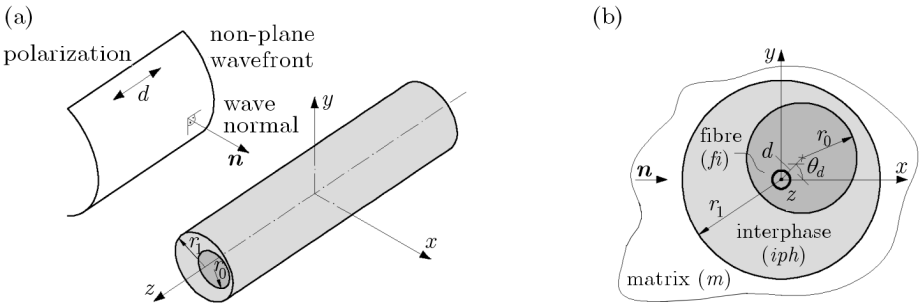


Fig. 3. Problem configuration, eccentric circular cylinder case; (a) 3D-view

As mentioned above, the only nontrivial displacement component for a SH wave scattering problem is the out of plane displacement w , if the SH wave propagates in the xy -plane and the axis of the obstacle is parallel to the z -axis as shown in Fig. 3b. This displacement takes the form

$$w(x, y, t) = w_0 \cos(\omega t + \alpha) = \text{Re} \{ \phi(x, y) e^{-i\omega t} \} \tag{2.3}$$

where the complex amplitude ϕ with $|\phi| = w_0$, $\text{Re} \{ \phi \} = w_0 \cos \alpha$ satisfies the Helmholtz equation

$$\Delta \phi + \frac{\omega^2}{c_T^2} \phi = 0 = \Delta \phi + k^2 \phi \tag{2.4}$$

which follows from introducing the ansatz Eq. (2.3) into Navier's equation (2.1). Herein the imaginary unit i and the circular frequency ω were introduced. By means of the shear modulus μ the stress components can be derived from the complex amplitude ϕ . In the following, the temporal factor $e^{-i\omega t}$ will be omitted.

3. An analytical approach to non-plane SH wave scattering

3.1. Concentric circular scatterer

The single scatterer problem at hand as well as the characterising variables in cylindrical coordinates are shown in Fig. 3b. The treatment of the single rovings as layered inclusions (and hence as scatterers for the impinging waves) was motivated in Section 1. In order to calculate the waves in the matrix, the interphase and the fibre, the solution of the Helmholtz equation in a circular coordinate system is sought. With the Laplacian in this coordinate system, equation (2.4) yields

$$\frac{\partial^2 \phi}{\partial r^2} + \frac{1}{r} \frac{\partial \phi}{\partial r} + \frac{1}{r^2} \frac{\partial^2 \phi}{\partial \theta^2} + k^2 \phi = 0 \quad (3.1)$$

cf. Morse and Feshbach (1953). Using the ansatz $\phi(r, \theta) = R(r)\Theta(\theta)$ and separation of constants leads to

$$\begin{aligned} \frac{\partial^2 \Theta}{\partial \theta^2} + n^2 \Theta &= 0 \\ r^2 \frac{\partial^2 R}{\partial r^2} + r \frac{\partial R}{\partial r} + (k^2 r^2 - n^2) R &= 0 \end{aligned} \quad (3.2)$$

where the latter equation is known as the Bessel differential equation. The solution of the Helmholtz equation in polar coordinates is a linear combination of cylindrical wave functions consisting of simple harmonics as the angular factor

$$\Theta_n(\theta) = c_{1n} \cos(n\theta) + s_{1n} \sin(n\theta) = C_{1n} e^{in\theta} + C_{2n} e^{-in\theta} \quad (3.3)$$

and the Bessel functions of various kinds as the radial factor

$$R_n(r) = A_{1n} J_n(kr) + iA_{2n} Y_n(kr) = C_{3n} H_n^{(1)}(kr) + C_{4n} H_n^{(2)}(kr) \quad (3.4)$$

cf. Pao and Mow (1971). Herein $H_n^{(1),(2)}(kr) = J_n(kr) \pm iY_n(kr)$ are the Hankel functions of the first and second kind, respectively. Due to the time dependency $e^{-i\omega t}$ used in this contribution the Hankel functions of the first kind $H_n^{(1)}(kr)$ represent outgoing waves – whereas in e.g. Skelton and James (1997), the time dependency is $e^{+i\omega t}$ and thus waves moving outward are calculated by means of the Hankel functions of the second kind $H_n^{(2)}(kr)$. For a more detailed description of the Bessel and Hankel functions, see e.g. Watson (1922).

By means of the shear modulus μ , the stress components can be derived from the complex amplitude of the displacement.

Often, plane waves are dealt with. As this special incoming wave is regular in the entire xy -plane and the only function in the general ansatz of Eq. (3.4) being regular throughout this plane is the Bessel function of the first kind, it is

$$\phi_{in} = \sum_{n=-\infty}^{\infty} A_n J_n(k_m r) e^{in\theta} \quad (3.5)$$

where the index m of the wave number k_m induces that the function is evaluated in the matrix region. The same holds for k_{iph} (inside the interphase) and k_{fi} (inside the fibre). According to Eq. (2.3), the Hankel functions of the first kind represent outgoing waves whereas the Hankel functions of the second kind count for waves moving inward. Hence, the scattered wave – which is directed outward with respect to the scatterer – can be described by the Hankel functions of the first kind

$$\phi_{sc} = \sum_{n=-\infty}^{\infty} B_n H_n^{(1)}(k_m r) e^{in\theta} \quad (3.6)$$

In the interphase, waves propagating in both directions occur and the complete ansatz including the Hankel functions of the first and second kind is needed

$$\phi_{iph} = \sum_{n=-\infty}^{\infty} \left[D_n H_n^{(1)}(k_{iph} r) + E_n H_n^{(2)}(k_{iph} r) \right] e^{in\theta} \quad (3.7)$$

The Hankel functions of the first and second kind are singular at the origin¹. Obviously, the refracted wave in the inner layer is regular, hence it is represented by the Bessel functions of the first kind

$$\phi_{fi} = \sum_{n=-\infty}^{\infty} C_n J_n(k_{fi} r) e^{in\theta} \quad (3.8)$$

As can be seen from Eqs. (3.5)-(3.8) all wave fields are composed of so the called wave expansion coefficients (A_n, \dots, E_n) and wave basis functions, that is Bessel functions of various kinds.

The entire field outside the scatterer, which will be evaluated in the given examples, is expressible as

$$\phi_{ent} = \phi_{in} + \phi_{sc} \quad (3.9)$$

For the problem at hand, a multi-layered elastic inclusion, the boundary conditions to be fulfilled are that the stress component σ_{rz} and the displacement ϕ are continuous across the interfaces. Within Section 4, a double-layered

¹Due to the singularity of the Bessel functions of the second kind $Y_n(kr)$ at $kr = 0$

elastic inclusion with boundaries at $r = r_0$ and $r = r_1$ will be investigated. Hence, the boundary conditions yield

$$\begin{aligned}
 \mu_m \left(\frac{\partial \phi_{in}}{\partial \xi} + \frac{\partial \phi_{sc}}{\partial \xi} \right) \Big|_{r=r_1} &= \mu_{iph} \frac{\partial \phi_{iph}}{\partial r} \Big|_{r=r_1} \\
 \mu_{iph} \frac{\partial \phi_{iph}}{\partial r} \Big|_{r=r_0} &= \mu_{fi} \frac{\partial \phi_{fi}}{\partial r} \Big|_{r=r_0} \\
 (\phi_{in} + \phi_{sc}) \Big|_{r=r_1} &= \phi_{iph} \Big|_{r=r_1} \\
 \phi_{iph} \Big|_{r=r_0} &= \phi_{fi} \Big|_{r=r_0}
 \end{aligned} \tag{3.10}$$

The spatial distribution of the entire wave according to equation (3.9) for a certain time t , that is, $\text{Re}\{\phi_{ent}e^{-i\omega t}\}$, is exemplarily shown in Fig. 4a. Herein and with the other plots use of the material properties given in Table 1 is made. In general, the main interest is finding maximum exposures of the material at hand – independently of time t . This information is provided by mapping the amplitude $|\phi_{ent}|$ as done in Fig. 4b for the present case of a concentric scatterer. In these figures, a plane wave of unit amplitude acts upon the concentric obstacle, the inclusions geometric configuration hereby is plotted within the diagram.

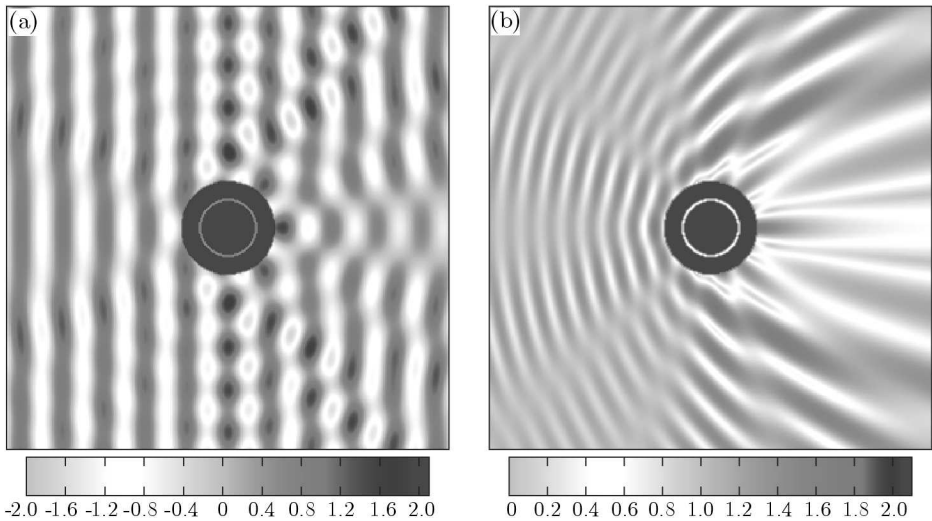


Fig. 4. Spatial distribution of displacement $\text{Re}\{\phi_{ent}e^{-i\omega t}\}$ (a) and $|\phi_{ent}|$ (b), concentric scatterer ($r_0 = 0.6r_1$, $d = 0$, and $\theta_d = 0$)

3.2. Specialisation to an eccentric circular scatterer

In real-life applications, the obstacles which scatter the incoming waves will not be concentric in general. Thus, the general ansatz developed in the precedent Section has to be extended with respect to eccentric scatterers. To fit the needs of eccentricities, for an n -layered scatterer n coordinate systems will be necessary. In this contribution $n = 2$ had been chosen. Herein the inner layer – the so called core – is shifted by d with respect to the outer layer. The line connecting the centres of both layers is then rotated by θ_d as shown in Fig. 3b. Hence, two (polar) coordinate systems are needed. The coordinate system connected with the inner layer (the fibre) is denoted with (r_{fi}, θ_{fi}) whereas the one of the interphase, i.e. the outer layer, is (r_{iph}, θ_{iph}) . The latter one will be used as the global coordinate system, e.g. for evaluating the waves in the matrix as well. Equations (3.5)-(3.8) for calculating the incoming, scattered and refracted waves thus have to be rewritten in terms of different coordinate systems. The ansatz functions for the fields inside the matrix, the interphase and the fibre then follow to

$$\begin{aligned}
 \phi_{in} &= \sum_{n=-\infty}^{\infty} A_n J_n(k_m r_{iph}) e^{in\theta_{iph}} \\
 \phi_{sc} &= \sum_{n=-\infty}^{\infty} B_n H_n^{(1)}(k_m r_{iph}) e^{in\theta_{iph}} \\
 \phi_{iph} &= \sum_{n=-\infty}^{\infty} \left[D_n H_n^{(1)}(k_{iph} r_{fi}) e^{in\theta_{fi}} + E_n H_n^{(2)}(k_{iph} r_{iph}) e^{in\theta_{iph}} \right] \\
 \phi_{fi} &= \sum_{n=-\infty}^{\infty} C_n J_n(k_{fi} r_{fi}) e^{in\theta_{fi}}
 \end{aligned} \tag{3.11}$$

It is emphasized that for the wave within the interphase both coordinate systems are used.

To fulfil the boundary and transition conditions as given with Eqs. (3.10), a formulation of all fields by means of the same coordinate system is adjuvant. With the addition theorem proved in Meixner and Schaefer (1954) it follows

$$\mathfrak{B}_n^{(j)}(kr_{fi}) e^{in(\theta_{fi} - \theta_{iph})} = \sum_{m=-\infty}^{\infty} \mathfrak{B}_{n+m}^{(j)}(kr_{iph}) J_m(kd) e^{in(\theta_{iph} - \theta)} \tag{3.12}$$

where $\mathfrak{B}_n^{(j)}(kr)$ with $j = 1, \dots, 4$ is the Bessel, Neumann or Hankel function of the first or second kind and order n . It is also known as Graf's addition theorem. By means of this addition theorem the two coordinate systems can be converted to each other.

The spatial distribution of the amplitude $|\phi_{ent}|$ due to a time-harmonic plane wave interacting with the present case of an eccentric scatterer is plotted in Fig. 5. Again, the scatterers geometric configuration is plotted within the diagram and the material properties according to Table 1 are used. For the eccentric case, especially in the first quadrant, enormous changes are observable in comparison with the concentric case shown in Fig. 4b. In these regions, the amplitude of the total wave by far exceeds the one of the incoming wave; the affected areas from which cracks may originate are plotted dark. Hence, the investigation of influences of the scatterers eccentricities to the behaviour of brittle matrices such as fine grained concrete is necessary.

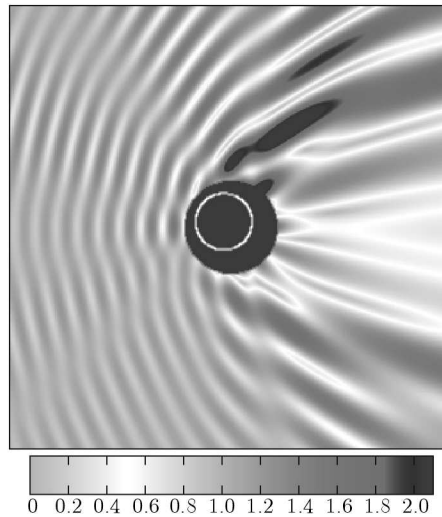


Fig. 5. Spatial distribution of the displacement amplitude $|\phi_{ent}|$, eccentric scatterer ($r_0 = 0.6r_1$, $d = 0.2r_1$, and $\theta_d = 4\pi/5$)

The extension to an inclusion of a more general shape, that is, an elliptical shape, is possible and was shown in e.g. Weber and Zastra (2009).

Substitution of the wave expansions for different coordinate systems into boundary and transition conditions (3.10) yields a linear system of equations for the coefficients B_n, \dots, E_n in terms of the expansion coefficients A_n of the incoming non-plane wave which will be determined in the next Section.

3.3. Modeling the incoming non-plane wave

This contribution deals with the scattering of non-plane SH waves. As an example, a cylindrical wave whose source is parallel to the axis of the scatterer is being looked at, cf. Fig. 3a. For determining the wave expansions

of the incoming wave ϕ_{in} its geometry is provided with Fig. 6, where the source of the incoming wave has the coordinates (r_s, θ_s) with respect to the global cylinder coordinate system. There, the obstacle – or rather, the center of the interphase – is situated. In general, a cylindrical wave propagating in the chosen matrix material follows the relation

$$\begin{aligned} \phi_{in} &= H_0^{(1)}(k_m \|\mathbf{r} - \mathbf{r}_s\|) \\ &= H_0^{(1)}\left(k_m \sqrt{r^2 + r_s^2 - 2rr_s \cos(\theta - \theta_s)}\right) = H_0^{(1)}(k_m R) \end{aligned} \tag{3.13}$$

with R being the distance between the particular point of observation and the source of the wave, see also Fig. 6. Again, the time dependency has been suppressed as throughout the whole paper.

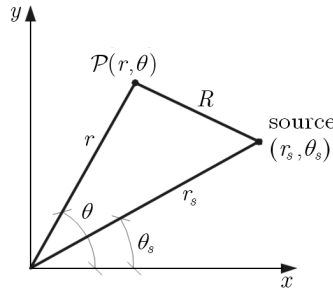


Fig. 6. Geometry of the source of a non-plane SH wave

This term has to be evaluated with respect to the global coordinate system as shown in Figs. 3b and 6. Two cases have to be taken into account: (i) $r < r_s$ and (ii) $r \geq r_s$. For the first case, the admissible wave functions are $J_n(k_m r)e^{in\theta}$, as ϕ_{in} has to be finite at $r = 0$ and periodic in 2π on θ . For the latter case, the admissible functions yield $H_n^{(1)}(k_m r)e^{in\theta}$, as ϕ_{in} has to represent waves propagating outward. Thus

$$\phi_{in} = \begin{cases} \sum_{n=-\infty}^{\infty} a_n H_n^{(1)}(k_m r_s) J_n(k_m r) e^{in(\theta - \theta_s)} & \text{for } r < r_s \\ \sum_{n=-\infty}^{\infty} a_n J_n(k_m r_s) H_n^{(1)}(k_m r) e^{in(\theta - \theta_s)} & \text{for } r \geq r_s \end{cases} \tag{3.14}$$

where the expansion coefficients a_n have to be determined now. For this, the source of the cylindrical wave is set into infinity, e.g. $(r_s = +\infty, \theta_s = 0)$.

Asymptotic formulas for the Hankel functions as given in Harrington (2001) may be used to obtain

$$\phi_{in} = H_n^{(1)}(k_m \|\mathbf{r} - \mathbf{r}_s\|) \xrightarrow{r_s \rightarrow +\infty, \theta_s = 0} \sqrt{\frac{2i}{\pi r_s}} e^{-ir_s} e^{ir \cos \theta} \tag{3.15}$$

and, consequently

$$\phi_{in} \xrightarrow{r_s \rightarrow +\infty, \theta_s = 0} \sqrt{\frac{2i}{\pi r_s}} e^{-ir_s} \sum_{n=-\infty}^{\infty} a_n i^n J_n(k_m r) e^{in\theta} \tag{3.16}$$

Herein, use of the expansion of a plane wave propagating in the positive x -direction

$$e^{ir \cos \theta} = \sum_{n=-\infty}^{\infty} A_n J_n(k_m r) e^{in\theta} = \sum_{n=-\infty}^{\infty} i^n J_n(k_m r) e^{in\theta} \tag{3.17}$$

was made, cf. Weyrich (1937). Obviously $a_n = 1$, thus leading

$$\phi_{in} = \begin{cases} \sum_{n=-\infty}^{\infty} H_n^{(1)}(k_m r_s) J_n(k_m r) e^{in(\theta - \theta_s)} & \text{for } r < r_s \\ \sum_{n=-\infty}^{\infty} J_n(k_m r_s) H_n^{(1)}(k_m r) e^{in(\theta - \theta_s)} & \text{for } r \geq r_s \end{cases} \tag{3.18}$$

Referring back to the ansatz given with Eq. (3.5), the wave expansion coefficients A_n for a cylindrical wave situated at (r_s, θ_s) are

$$A_n = \begin{cases} H_n^{(1)}(k_m r_s) e^{in(-\theta_s)} & \text{for } r < r_s \\ J_n(k_m r_s) e^{in(-\theta_s)} & \text{for } r \geq r_s \end{cases} \tag{3.19}$$

which implies changes within the wave basis functions of the incoming wave as well. As the final step, these A_n may be scaled in such a way that ϕ_{in} has unit amplitude at a certain point² in free space – e.g. at $(r = r_1, \theta = \pi)$, that is, at the nearest point of the obstacle facing the source of the incoming wave ϕ_{in} , at the origin $(r = 0, \theta = 0)$ or at $(r = r_1, \theta = 0)$ – the point of the scatterer having the longest distance to the source of the cylindrical wave.

Figures 7a,b show the spatial distribution of both the current displacement field $\text{Re}\{\phi_{ent} e^{-i\omega t}\}$ at an arbitrary time t and the displacement amplitude $|\phi_{ent}|$ for an eccentric double-layered scatterer due to a cylindrical wave. To ensure a better comparability with Figs. 4 and 5, the incoming cylindrical wave ϕ_{in} has unit amplitude at the centre of the obstacle. The material properties refer to Table 1.

²In fact all points within the xy -plane lying in the material and having the same distance from the source will have equal amplitudes

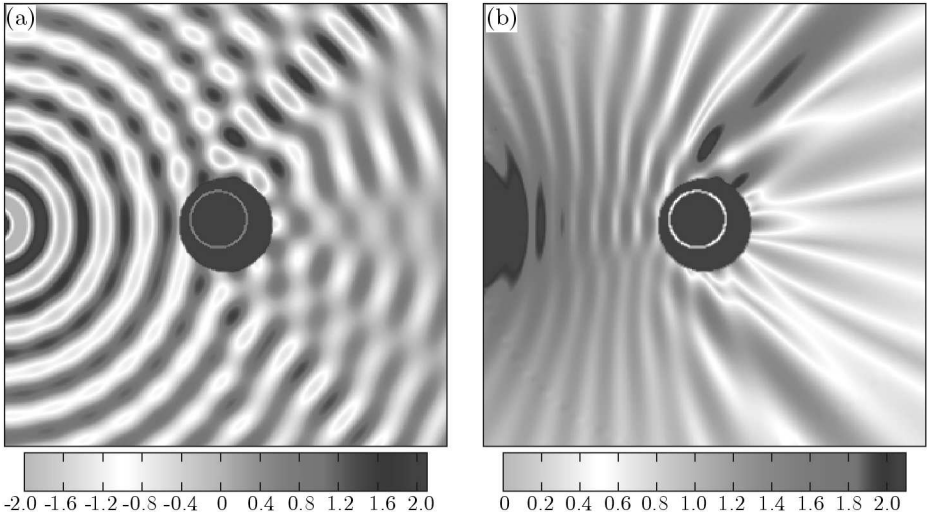


Fig. 7. Spatial distribution of the displacement $\text{Re}\{\phi_{ent}e^{-i\omega t}\}$ (a) and $|\phi_{ent}|$ (b), eccentric scatterer ($r_0 = 0.6r_1$, $d = 0$, and $\theta_d = 4\pi/5$), due to a non-plane SH wave

4. Numerical example

In this Section, some numerical results for TRC based on the analytical solutions of the precedent Sections are presented. The investigations deal with the displacement distribution in the vicinity of a double-layered obstacle. The radius of the scatterers outer layer is r_1 , whereas the radius of the inner layer is $r_0 = 0.6r_1$, see also Figs. 4, 5 and 7. Between both, the interphase is arranged, the fibre is represented by the inner layer. Carbon fibres were used as reinforcement of the fine-grained concrete. The constituents properties are listed in Table 1 und were taken from SFB 528. The scatterer is subjected to a non-planar incident SH wave as given with Eq. (3.18) whose source is set at ($r_s = 5a$, $\theta_s = \pi$). The intensity of the source is scaled in such a way that the incoming non-plane wave would reach unit amplitude at ($r = 0$, $\theta = 0$), thus at the centre of the obstacle.

Table 1. Material properties of a certain type of TRC

Constituent	Matrix	Carbon fibre	Interphase
ρ [kg/m ³]	2 160	1 760	1 500
μ [GPa]	12	97	1.17
ν	0.2	0.0	0.49
c_T [m/s]	2 340	7 440	880

In mechanical sense, the scattering of non-plane elastic SH waves is influenced by three geometric parameters, that is, the core size r_0 with respect to r_1 , the offset d and the orientation angle θ_d as introduced in Fig. 3b. As the investigations in this contribution were motivated by the requirements of TRC, the range of the core size is limited³ and so is the offset⁴. Hence, the focus of the investigations lies on varying angles θ_d , the orientation angle. Additionally, the behaviour of the chosen scatterer for different frequency regimes is being looked at. For both fixed eccentricity and frequency, the total displacement field $\text{Re}\{\phi_{ent}e^{-i\omega t}\}$ for a certain time t as well as the spatial distribution of its amplitude $|\phi_{ent}|$ due to a cylindrical wave is shown in Figs. 7a,b.

In addition to these aforementioned evaluations, the scattering behaviour can be exploited well by investigating the amplitude of the entire wave at a certain distance from the scatterer for different frequency regimes. In this contribution, the chosen distance is $r = 4r_1$ referring to the centre of the outer layer. In Figs. 8 and 9, these amplitudes are sketched within a polar plot. Each polar plot contains the (normalised) amplitudes of the entire wave ϕ_{ent} for the dimensionless frequencies $k_m r_1 = \{1, 5, 10\}$. Please note that these diagrams do not provide classical directivity patterns, as not the scattered wave ϕ_{sc} is plotted but the entire wave ϕ_{ent} .

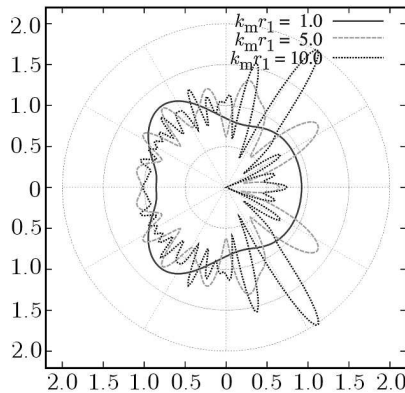


Fig. 8. Polar plot of $|\phi_{ent}|$ at a distance $r = 4r_1$ with $d = 0$ (concentric scatterer)

As can be readily reconstructed from Fig. 7a, the amplitude of the incoming wave (of course) decreases with increasing distance from its source – thus showing a main difference between planar waves as given in Fig. 4a. Hence,

³The core size is set constant to $r_0 = 0.6r_1$, a useful range should be $0.6r_1 \leq r_0 \leq r_1$

⁴The offset is $d = 0.2r_1$ for all calculations performed, a useful range should be $0 \leq d \leq (r_1 - r_0)$

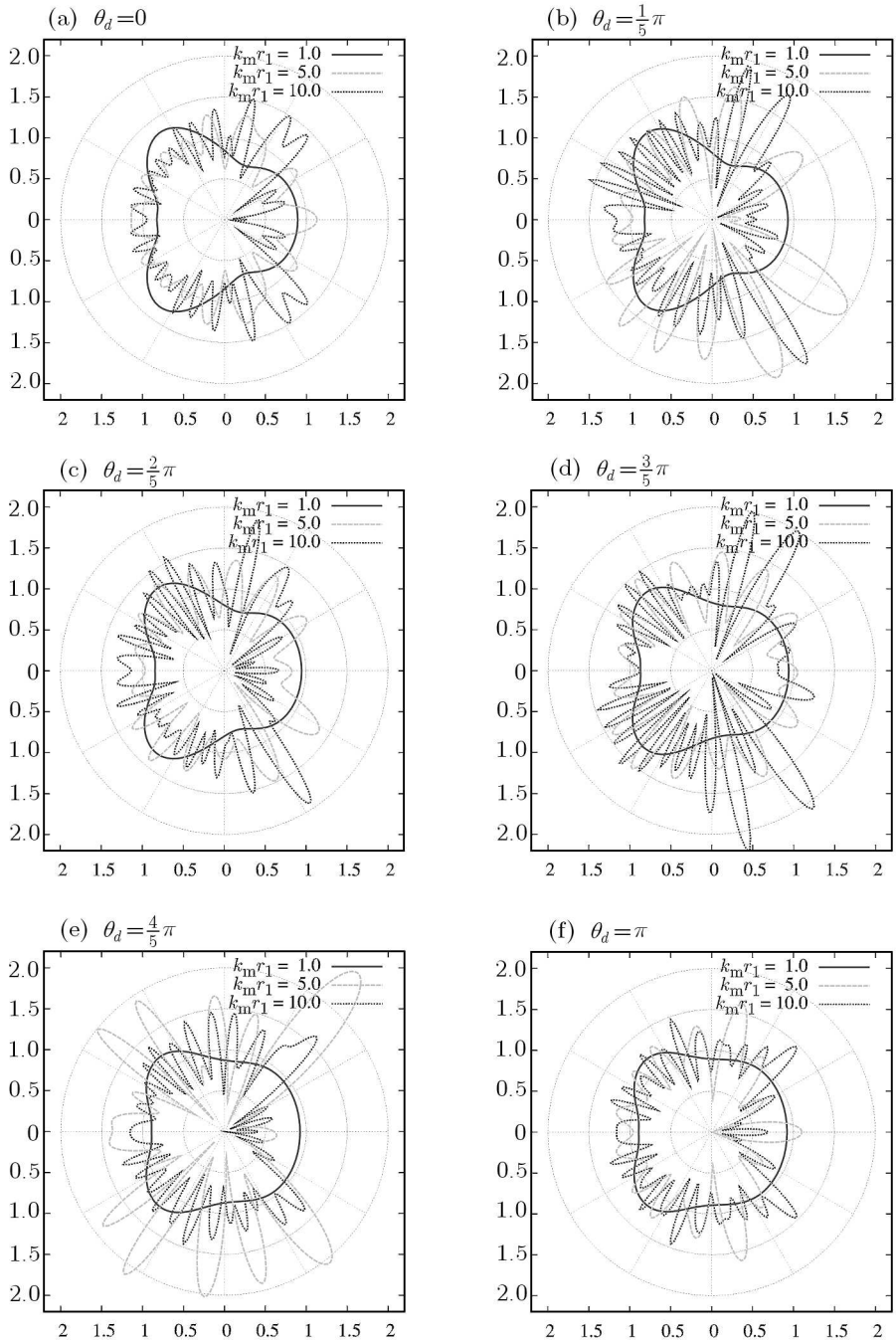


Fig. 9. Polar plot of $|\phi_{ent}|$ at a distance $r = 4r_1$ with $d = 0.2r_1$

a normalisation of the entire field at each point in free space lying on the circumferential line with distance $r = 4r_1$ from the scatterers origin by the respective maximum value – that is

$$\frac{|\phi_{ent}(r = 4r_1, \theta, k_m)|}{|\phi_{ent}(r = 4r_1, \theta, k_m)|_{max}}$$

as done in Weber and Zastrau (2010) is not helpful if the relation of the entire wave to the incoming one is of interest. Due to this fact the authors decided to normalise each field point circumscribing the scatterer at a distance from $r = 4r_1$ measured from the origin by the amplitude of the incoming non-plane wave at this particular point

$$\frac{|\phi_{ent}(r = 4r_1, \theta, k_m)|}{|\phi_{in}(r = 4r_1, \theta, k_m)|}$$

Thus, if no obstacle was present⁵ this quotient would equal 1 for all field points, hence yielding to a circle with radius 1 in the polar plots in Figs. 8 and 9. As a reference, Fig. 8 shows the normalised amplitude of the entire wave on a circumferential line around the concentric scatterer ($d = 0$).

To show the remarkable influence of eccentricities to the wave scattering behaviour of TRC, the inner layer is then shifted by $d = 0.2r_1$ and rotated by $\theta_d = \{0, \frac{1}{5}\pi, \frac{2}{5}\pi, \frac{3}{5}\pi, \frac{4}{5}\pi, \pi\}$ with respect to the positive x -axis, as defined in Fig. 3b. As can be seen from Figs. 9a-9f for a fixed core size and offset the scattering behaviour strongly depends on the frequency of the incoming non-plane SH wave. For low (dimensionless) frequencies, e.g. $k_m r_1 = 1$, the normalised amplitude of the entire wave ϕ_{ent} oscillates around 1 with θ , where the oscillating “frequency”⁶ is quite low. As expected, the normalised amplitude does not vary that much for $k_m r_1 = 1$. Additionally it clearly can be seen that the changes in the graphs curvature even decrease with increasing orientation angle θ_d . This is due to the fact that for increasing θ_d the scattering gets more and more forward, see Weber and Zastrau (2010), thus reducing the peaks in the backward direction at $\theta \approx \pm \frac{3}{4}\pi$. Investigating the medium frequency regime $k_m r_1 = 5$, yields that the “frequency” of the oscillatory structure of the plotted graph is higher than in the regime $k_m r_1 = 1$. It is also apparent that the ratios

$$\frac{|\phi_{ent}(r = 4r_1, \theta, k_m)|}{|\phi_{in}(r = 4r_1, \theta, k_m)|} > 1.5$$

⁵Or the inclusion would have the same material properties as the surrounding matrix

⁶Of the varying normalised amplitude

mainly occur for the orientation angles $-\frac{1}{5}\pi \leq \theta_d \leq \frac{1}{5}\pi$ and $\frac{4}{5}\pi \leq \theta_d \leq \frac{6}{5}\pi$. Thus, small deviances of the position of the inner core with respect to the x -axis should be omitted. For $k_m r_1 = 10$, it can be stated that the oscillations within the scattering pattern have an even higher “frequency” as in the two cases investigated before. The second observation is that there seems no clear connection between small orientation angles θ_d and enlarged amplitudes of ϕ_{ent} which was revealed for $k_m r_1 = 5$. It is conjectured that the higher the dimensionless frequency $k_m r_1$ the more chaotic the scattering patterns are. Hence, further investigations are necessary.

Concerning the shielding of the incoming wave, it can be stated that the entire waves amplitude in the forward direction ($\theta = 0$) as conjectured decreases with increasing frequency of the incoming wave. The previous numerical results further showed that within the design process the engineer should assume displacement amplitudes in the vicinity ($r = 4r_1$) of a single obstacle of radius r_1 due to scattering approximately reaching twice the amplitude of the incoming wave, at least in the region $\theta = \pm(\frac{1}{6}\pi, \dots, \frac{5}{6}\pi)$.

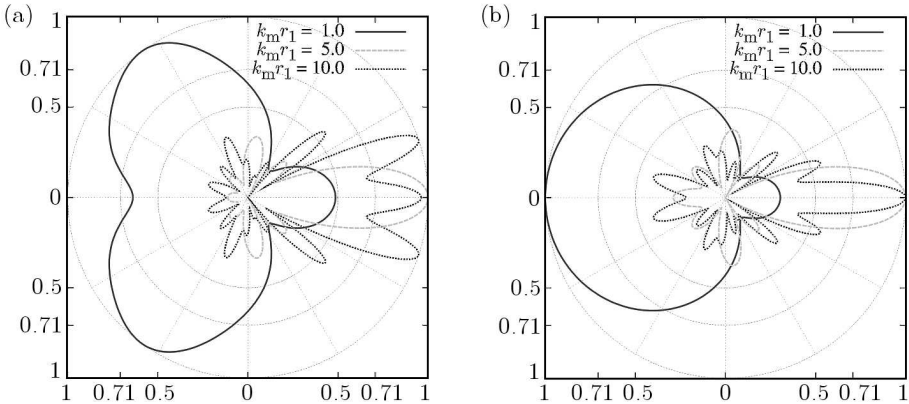


Fig. 10. Polar plot of $|\phi_{sc}|$ at a distance $r = 4r_1$ with $d = 0.2r_1$, $\theta_d = \pi$;
(a) non-plane wave, (b) plane wave

Obviously, the directivity pattern – that is, the polar plot of only the scattered field ϕ_{sc} (normalised by its respective maximum value) which is provided in Fig. 10a – for the example of a non-plane wave highly differs from the one obtained for the plane wave case as given in Fig. 10b. For this, two main reasons can be identified: firstly, the wave chosen in this contribution propagates cylindrically outward with respect to its centre, thus more and more decreasing its amplitude due to energy conservation. Hence, the incoming wave at the surface of the obstacle in the forward direction of the scatterer will have a lower amplitude than at the surface in the backward direction – and so

will the scattered wave. These difficulty can be overcome by means of proper normalisation as shown in Figs. 9a-9f. The second reason for the remarkable changes in the directivity patterns and related graphs is the drastically different distribution of the incoming wave field at the surface of the obstacle due to the additional curvature of the wavefront of the incoming cylindrical wave. On the other hand, this is exactly the reason for the investigations presented here. It is evident that with increasing distance R of the scatterer from the source of the incoming wave, with decreasing size of the obstacle or with increasing k_m the differences related to the curvature of the wavefront of the incoming wave will reduce. First signs of which can be seen from Fig. 10a for the high-frequency regime when comparing them with the results obtained for the plane wave case in Fig. 10b.

5. Conclusions

Efficient investigations concerning the scattering behaviour of non-plane elastic SH waves due to a single but multi-layered eccentric obstacle can be performed by the derived analytical approach. It opens up the possibility for fast calculations of different geometric configurations as they occur with stochastic or fuzzy-stochastic analyses. Additionally, the obtained results may be coupled to standard procedures as BEM, thus avoiding – for special cases – the use of FEM or XFEM.

Numerical calculations were performed for TRC and showed regions with a tremendous increase of the materials exposures due to an incoming wave even in the single scatterer case. These exposures exceed the ones known from concentric scatterers with comparable material properties by far. The conjecture that the scattering of non-plane waves leads to different results compared with incoming plane waves could be confirmed. These differences decrease with the increasing ratio R/r_1 , where R is the distance of the scatterer from the source of the incoming wave and r_1 the outer radius of the obstacle itself, and with increasing k_m . Hereby, the geometric property R/r_1 in the limiting case $R/r_1 \rightarrow \infty$ directly leads to plane waves. It is thus apparent that especially in the vicinity of non-plane wave sources the procedure proposed in this contribution is essential for studying the wave scattering behaviour, whereas in the far field region a “reduced” approach with incoming plane waves – which means reduced numerical effort – may be accurate enough.

A profound knowledge concerning the wave scattering behaviour of composite materials at the micro- and meso-scale, which may be obtained by means

of the presented procedure, allows the engineer to derive proper material models at the macro- or structural scale. On the other hand, materials having certain wave-scattering-properties may be constructed within an inverse process. However, this implies manufacturing of these materials under laboratory conditions. Hence, this work is a contribution to prevent structures from hazardous responses to dynamic loads.

References

1. ACHENBACH J.D., 1973, *Wave Propagation in Elastic Solids*, North-Holland, New York
2. CAI L.-W., 2004, Multiple scattering in single scatterers, *J. Acoust. Soc. Am.*, **115**, 3, 986-995
3. HARRINGTON R.F., 2001, *Time-Harmonic Electromagnetic Fields*, Wiley & Sons, New York
4. LEPENIES I., 2007, Zur hierarchischen und simultanen Multi-Skalen-Analyse von Textilbeton, Ph.D. Thesis, Technische Universität Dresden
5. MEIXNER J., SCHAEFKE F.W., 1954, *Mathieusche Funktionen und Sphäroidfunktionen*, Springer, Heidelberg
6. MORSE P.M., FESHBACH H., 1953, *Methods of Theoretical Physics*, McGraw-Hill, New York
7. ORTLEPP R., CURBACH M., 2009, Verstärken von Stahlbetonstützen mit textilbewehrtem Beton, *Beton- und Stahlbetonbau*, **104**, 10, 681-689
8. PAO Y.-H., MOW C.-C., 1971, *Diffraction of Elastic Waves and Dynamic Stress Concentrations*, Crane Russak & Co, New York
9. SKELTON E.A., JAMES J.H., 1997, *Theoretical Acoustics of Underwater Structures*, Imperial College Press, London
10. WATSON G.N., 1922, *A Treatise on the Theory of Bessel Functions*, Cambridge University Press, Cambridge
11. WEBER W., ZASTRAU B.W., 2009, On SH wave scattering in TRC – Part I: Concentric elliptical inclusion, *Machine Dynamics Problems*, **33**, 2, 105-118
12. WEBER W., ZASTRAU B.W., 2010, On the influence of asymmetric roving configurations on the wave scattering behaviour of TRC, *2nd ICTRC Textile Reinforced Concrete*, 271-281
13. WEYRICH R., 1937, *Die Zylinderfunktionen und ihre Anwendungen*, Teubner, Leipzig

Niepłaskie rozpraszanie fal od kołowego mimośrodowo osadzonego wtrącenia w materiale – część I: fale SH

Streszczenie

W pracy przedstawiono analityczny formalizm zagadnienia rozpraszania fal na pojedynczym, wielowarstwowym wtrąceniu materiałowym w izotropowej, jednorodnej strukturze osnowy poddanej działaniu niepłaskich fal spolaryzowanych w płaszczyźnie poziomej (fale typu SH). Założono, że wtrącenie ma kołowy kształt, a jego warstwy są rozmieszczone mimośrodowo. Zamieszczono rezultaty symulacji numerycznych na przykładzie nowego materiału budowlanego, jakim jest beton wzmocniany tekstyliami. Pokazano efekt ekranowania i wzmocnienia fal SH w takiej strukturze.

Manuscript received November 28, 2010; accepted for print February 18, 2011